Dynamical quantum phase transitions in a spinor Bose-Einstein condensate and criticality enhanced quantum sensing

Lu Zhou [1,*] Jia Kong,[2] Zhihao Lan,[3,†] and Weiping Zhang [4,5,6,7,‡]

[1]*State Key Laboratory of Precision Spectroscopy, Department of Physics, School of Physics and Electronic Science, East China Normal University, Shanghai 200241, China*
[2]*Department of Physics, Hangzhou Dianzi University, Hangzhou 310018, China*
[3]*Department of Electronic and Electrical Engineering, University College London, Torrington Place, London WC1E 7JE, United Kingdom*
[4]*School of Physics and Astronomy, and Tsung-Dao Lee Institute, Shanghai Jiao Tong University, Shanghai 200240, China*
[5]*Shanghai Research Center for Quantum Sciences, Shanghai, 201315, China*
[6]*Collaborative Innovation Center of Extreme Optics, Shanxi University, Taiyuan, Shanxi 030006, China*
[7]*Shanghai Branch, Hefei National Laboratory, Shanghai 201315, China*

Quantum phase transitions universally exist in the ground and excited states of quantum many-body systems, and they have a close relationship with the nonequilibrium dynamical phase transitions, which however are challenging to identify. In the system of spin-1 Bose-Einstein condensates, though dynamical phase transitions with correspondence to equilibrium phase transitions in the ground state and uppermost excited state have been probed, those taking place in intermediate excited states remain untouched in experiments thus far. Here we unravel that both the ground- and excited-state quantum phase transitions in spinor condensates can be diagnosed with dynamical phase transitions. A connection between equilibrium phase transitions and nonequilibrium behaviors of the system is disclosed in terms of the quantum Fisher information. We also demonstrate that near the critical points parameter estimation beyond the standard quantum limit can be implemented. This work not only advances the exploration of excited-state quantum phase transitions via a scheme that can immediately be applied to a broad class of few-mode quantum systems, but also provides a new perspective on the relationship between quantum criticality and quantum enhanced sensing.

I. INTRODUCTION

In quantum many-body systems, excited-state quantum phase transitions (ESQPTs) can be more appealing compared with quantum phase transitions (QPTs), which refer to quantum criticality aroused in ground states [1]. ESQPTs extend the study of criticality to excitation spectra and have recently been disclosed in several quantum systems [2–7]. The criticalities associated with QPTs and ESQPTs can reveal themselves by nonequilibrium quantum phenomena, especially the dynamical phase transition (DPT) [8–19].

DPT is characteristic of the nonanalyticity in the Loschmidt echo rate function after quantum quench. A more experimentally accessible clue would be that physical quantities become nonanalytical as a function of time, such as the order parameter. It is still an open question on the universal correspondence between DPTs and QPTs, also ESQPTs.

---

*lzhou@phy.ecnu.edu.cn
†lanzhihao7@gmail.com
‡wpz@sjtu.edu.cn

In this work, taking the system of an antiferromagnetic spin-1 Bose-Einstein condensate (BEC) as an example, we illustrate the relationship between DPTs and equilibrium phase transitions. Superfluidity and magnetism are simultaneously achieved in a spinor BEC. Due to the interplay between intrinsic spin-dependent collision interactions and Zeeman energy splittings controlled by an external field, the system of a spinor condensate features a rich phase diagram both in the ground and excited states [20–22]. QPTs have been experimentally explored in the ground state of spin-1 condensates with ferromagnetic [23] or antiferromagnetic [24–26] interaction, which show interesting phenomena and applications, such as nontrivial dynamics in space [27,28], the Kibble-Zurek mechanism [29,30], preparation of macroscopic many-body entangled states [31], and surpassing the standard quantum limit (SQL) [32]. The authors in [33] showed that the phase transition points can be mapped out through DPT with measurement on the long-time average of fractional population, which was used to explore the ESQPT taking place in the uppermost energy level [34]. However, little effort has been devoted to the study of ESQPTs in the intermediate excited states until recently; a topological order parameter was proposed to characterize ESQPTs in a spinor BEC [35], whose measurement relies on the precise operation after one period of spin oscillation and thus can be experimentally challenging. Besides that, a mimic of ESQPTs in spinor condensates has

also been studied in Raman-dressed spin-orbit coupled BECs [36,37].

Though diverging oscillation periods [38] and winding number changing [35] are regarded to be linked to ESQPTs, they can also be explained within mean-field theory, and an unambiguous quantum signature of ESQPTs has not been identified to our knowledge. On the other hand, only recently has the spin singlet (S) ground state been experimentally prepared and observed in an antiferromagnetic spinor BEC [39], since its first prediction in the 1990s [40]. It is interesting to explore the DPTs between the S state and other ground states. Here, we show that both the QPTs and ESQPTs can be captured with DPT. Specifically, the nonequilibrium dynamics of DPT could be characterized by the quantum Fisher information (QFI), which is intimately related to Loschmidt echoes [41–45].

Criticality can serve as a valuable resource for quantum metrology, finding applications in estimation of external parameters at high sensitivity [46–60]. Enhanced estimation on the control parameter in a spinor condensate has been studied [61,62], based on equilibrium phase transitions in the ground states. It is time consuming to prepare critical ground states via typical adiabatic evolution, especially in an antiferromagnetic spin-1 condensate due to the closing energy gap between ground and first-excited states [63]. Motivated by recent study that DPTs can be harnessed for quantum enhanced sensing in a closed quantum system [64], we explore the prospect of parameter estimation in a spinor condensate with DPTs.

II. QPTs AND ESQPTs IN AN ANTIFERROMAGNETIC SPIN-1 CONDENSATE

We consider a spinor BEC of N atoms with hyperfine spin $F = 1$. Within the single-mode approximation, which enables the internal spin dynamics being isolated from the external center-of-mass motion, the system is governed by the Hamiltonian ($\hbar = 1$) [21,22]

$$\hat{H} = \frac{c}{2N}\hat{S}^2 - q\hat{N}_0, \quad (1)$$

where c and q characterize the interspin and effective quadratic Zeeman energies, respectively. Here, $\hat{S}_{i=x,y,z} = \hat{a}_\alpha^\dagger S_i^{\alpha\beta} \hat{a}_\beta$ are spin-1 vector operators with $\hat{a}_m$ ($\hat{a}_m^\dagger$) the bosonic annihilation (creation) operators for the magnetic sublevels $m = 0, \pm 1$ and $S_{i=x,y,z}$ the spin-1 matrices (the indices α, β are summed over m). The atom number operators $\hat{N}_m = \hat{a}_m^\dagger \hat{a}_m$ and $N = \sum_m \hat{N}_m$. While q can only take a positive value if it is induced by an external magnetic field B, i.e., $q \propto B^2$, it can be tuned to both positive and negative values via microwave dressing [38,65,66]. In the following, we will concentrate on the antiferromagnetic spinor condensate ($c > 0$) with zero magnetization.

A sketch of the system phase diagram is given in Fig. 1, which is obtained via exact diagonalization of Hamiltonian (1) with an atom number $N = 300$. It will be helpful to rewrite Hamiltonian (1) in a more generic form as $\hat{H} = \hat{H}_0 + q\hat{H}_q$, and ground-state properties can be recognized as results aroused by the competition between $\hat{H}_0$ and $\hat{H}_q$: (i) For $|q| \gg c$, the ground state is dominated by $\hat{H}_q = \hat{N}_0$, thus resulting in the polar (P) state and twin-Fock (TF) state, with
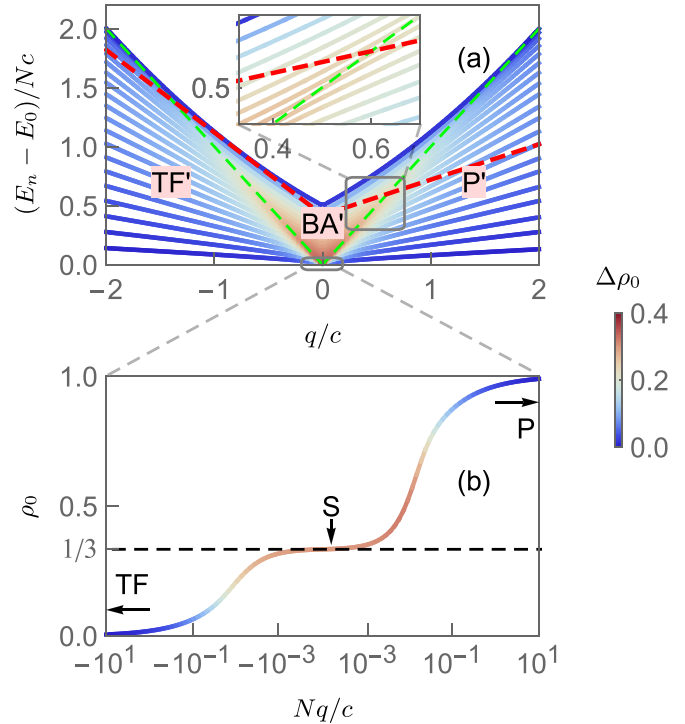

FIG. 1. Quantum phases of an antiferromagnetic spin-1 BEC of $N = 300$ atoms with zero magnetization, using the number variance $\Delta\rho_0$ in spin-0 component. (a) Excited spectra with every 15 eigenvalues. The green dashed lines are the ESQPT lines. The red dashed lines represent the mean-field energy $\mathcal{E}$ of a CSS (4) with $\rho_0 = 0.7$. (b) Ground state varies with q from TF, S to P.

$\rho_0 \equiv \frac{\langle \hat{N}_0 \rangle}{N} = 1$ and 0, respectively, in the positive and negative q direction, associated with vanishing variance $\Delta\rho_0 \equiv \frac{\Delta\hat{N}_0}{N}$; (ii) $\hat{H}_0 \propto \hat{S}^2$ restores SO(3) symmetry in a narrow window of $|q| < \frac{c}{N^2}$, resulting in the S ground state with $S = 0$ for even N. State S is massively entangled typical of large variance $\Delta\rho_0$, and with atoms evenly distributed among the magnetic sublevels, representing a three-fragment mesoscopic quantum state with $\rho_0 = \frac{1}{3}$. In the thermodynamical limit of $N \to \infty$, the S state disappears and the QPT is characterized by a first-order phase transition between the P and TF states.

The excited eigenspectra display a cumulation of avoided crossings along $E = E_g + |q|$ [green dashed lines in Fig. 1(a); see the inset for a enlarged view], which correspond to singularities in the density of states under the thermodynamical limit. Thus we refer to the lines as the ESQPT lines and the variances $\Delta\rho_0$ of the eigenstates in the vicinity of these lines also achieves maximum values. The three phases separated by these lines are labeled as P′, TF′, and BA′ (broken axisymmetry). While P′ and TF′ are named according to the corresponding ground states, BA′ is named after the highest-energy BA state [23,67], which possesses a transverse magnetization perpendicular to the applied external field and thus breaks the SO(2) axisymmetry.

III. RELATION BETWEEN DPTs AND THE QFI

To explore the relation with equilibrium phase transitions, we characterize DPTs with the QFI, which is defined as the

fidelity susceptibility [64,68,69]

$$F_Q(q, t) = -4 \frac{\partial^2 F(q, \delta q, t)}{\partial(\delta q)^2}\Big|_{\delta q \to 0}, \quad (2)$$

where the fidelity $F(q, \delta q, t) \equiv |\langle\psi(q,t)|\psi(q + \delta q, t)\rangle| = |\langle\psi_0|e^{i\hat{H}(q)t}e^{-i\hat{H}(q+\delta q)t}|\psi_0\rangle|$ is actually the Loschmidt echo, and it measures the revival of a state $|\psi_0\rangle$ experiencing time-forward propagation under $\hat{H}(q)$ followed by reversed evolution with $\hat{H}(q + \delta q)$. One can expect that when the system becomes critical with $q \to q_c$, the quantum state evolution behaves singularly and exhibits quite distinct results even for a small δq, resulting in prominent decrease of the fidelity and a high F_Q. An approximate long-time secular analytic expression for the QFI can be found in Appendix B as

$$F_Q(q, t) \simeq 4t^2\left[\sum_n |c_n|^2 (H_q^n)^2 - \left(\sum_n |c_n|^2 H_q^n\right)^2\right], \quad (3)$$

where $c_n = \langle\psi_n|\psi_0\rangle$ is the projection of the initial state $|\psi_0\rangle$ onto the eigenstates $|\psi_n\rangle$ of the Hamiltonian (1), and $H_q^n = \langle\psi_n|\hat{H}_q|\psi_n\rangle$. Equation (3) indicates that a peak in the QFI can be attributed to either enhanced fluctuations in the order parameter ($H_q^n = N_0^n = \langle\psi_n|\hat{N}_0|\psi_n\rangle$) or those in the overlaps between the initial state and the eigenstates.

To achieve the correspondence between DPTs and equilibrium phase transitions, one would expect that the overlap between the initial state and system eigenstates $|c_n|^2$ has similar singular distribution to the order parameter around the energy E_n^c (an excited eigenstate will however give zero value of F_Q). Among many possible choices of initial state, we propose to use coherent spin state (CSS) $|\zeta\rangle^{\otimes N}$, with $|\zeta\rangle \equiv \sum_m \zeta_m|m\rangle$ and $\zeta = (\sqrt{\frac{1-\rho_0+\rho_m}{2}}e^{i\chi_+}, \sqrt{\rho_0}, \sqrt{\frac{1-\rho_0-\rho_m}{2}}e^{i\chi_-})^T$, where $\rho_m = \frac{N_1-N_{-1}}{N}$, $\chi_\pm = \frac{\theta_s \pm \theta_m}{2}$ with $\theta_{s(m)}$ the spinor phase and magnetization phase, respectively. CSS can be visualized by casting the corresponding mean-field phase diagram at different q into the spin-nematic phase sphere $\{S_\perp, Q_\perp, 2\rho_0 - 1\}$ with the transverse spin $S_\perp = \sqrt{\langle\hat{S}_x\rangle^2 + \langle\hat{S}_y\rangle^2}$ and transverse off-diagonal nematic moment $Q_\perp = \sqrt{\langle\hat{Q}_{xz}\rangle^2 + \langle\hat{Q}_{yz}\rangle^2}$ [70], where the quadrupole operators $\hat{Q}_{ij} \equiv \hat{a}_\alpha^\dagger[S_iS_j + S_jS_i - (4/3)\delta_{ij}]\hat{a}_\beta$ (the indices α, β are summed over m). In the thermodynamical limit, the dynamics of an initial CSS is characterized by its equal-energy trajectories of the spin-nematic component on the sphere. As shown in Fig. 2(a), on the positive q side it can be tuned from that in the P′ phase space (white line), the separatrix dividing the BA′ and P′ phase space (red line linked to the unstable hyperbolic point $n_0 = 0$), and that in the BA′ phase space (yellow line). Similar transitions from BA′ to TF′ phase can take place at $q < 0$. The spin dynamics can be denoted as coherent oscillation with varying amplitude and period, while for a CSS which is initially localized at the separatrix, it will become singular with diverging period [71].

Taking the CSS with $\{\rho_0 = 0.7, \rho_m = 0, \theta_s = \theta_m = 0\}$ as an example [whose mean-field energy $\mathcal{E}$ is shown as the red dashed line in Fig. 1(a)], at the intersections with the ESQPT line on $q = 0.6c$ ($\mathcal{E} = \mathcal{E}_c = E_n^c|_{N\to\infty}$), for a finite system it represents a distribution on the surface of the spin-nematic

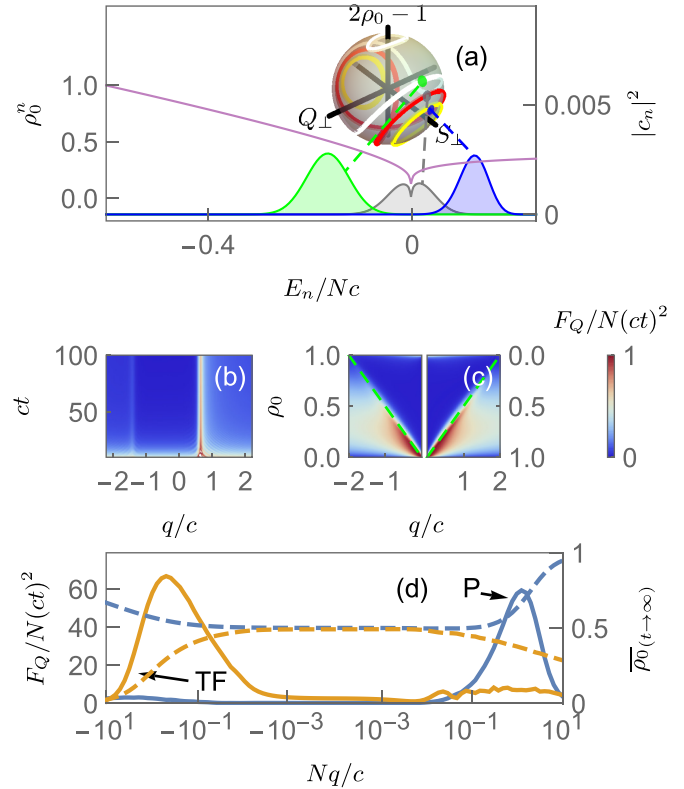FIG. 2. (a) Slice of the phase diagram Fig. 1 at $q = 0.6c$ cast into the $\{S_\perp, Q_\perp, 2\rho_0 - 1\}$ spin-nematic sphere, where the separatrix ($\mathcal{E} = \mathcal{E}_c$, red line) separates trajectories in the BA′ phase ($\mathcal{E} > \mathcal{E}_c$, yellow) from those in the P′ phase ($\mathcal{E} < \mathcal{E}_c$, white), and a distribution (the blue, gray, and green circles) represents a CSS on the sphere with $\rho_0 = 0.6, 0.7, 0.8$, respectively. Eigenstate overlap $|c_n|^2$ with these CSSs are plotted (right axis), associated with the eigenstate normalized population ρ_0^n (left axis, purple curve). (b) Time evolution of the QFI F_Q as a function of q. (c) Phase diagram in the q-ρ_0 plane computed with F_Q at $ct = 10^3$. Green dashed curves refer to ESQPT lines. (d) F_Q calculated at $ct = 10^3$ versus q (left axis) with an initial P state (blue curve), and an initial TF state (brown curve). The corresponding dashed curves represent time-averaged population in spin-0 component $\overline{\rho_0(t)}|_{t\to\infty}$ (right axis).

sphere with uncertainty equal to SQL ($1/\sqrt{N}$) and center located on the separatrix, which is marked as a gray circle in Fig. 2(a). Since the mean-field energy of the CSS equals that of the critical saddle point, it is closer to the eigenstate at which ESQPT takes place as compared with other higher (blue circle for $\rho_0 = 0.6$) or lower energy CSS (green circle for $\rho_0 = 0.8$), resulting in the nonanalytical features of $|c_n|^2$ at E_n^c (gray line), which are not captured by other CSSs in the P′ or BA′ phase (green line and blue line).

We use the CSS as the initial state to simulate QFI (2) with atom number $N = 1000$ (see Appendix A for details about numerical methods) and present the dynamical behavior of $F_Q/N(ct)^2$ versus q in Fig. 2(b), where the normalization with respect to t^2 is chosen to absorb the expected long-time growth of $F_Q \propto t^2$. Around the critical points $q_c = -1.4c$ and $0.6c$, a prominent increase in the QFI can be observed, which correspond to the cases where the CSS is centered on the

separatrix, linked to the saddle point $\rho_0 = 1$ and $\rho_0 = 0$, respectively. This suggests that the quantum dynamics exhibits abrupt change around the critical points and thus the QFI can serve as an indicator of ESQPTs. These two QFI peaks in the long-time limit separate the parameter space into three regions, i.e., the BA$'$, TF$'$, and P$'$ phase, respectively. Apart from the phase transition region, the QFI displays damped oscillations.

Motivated by the feasibility that ESQPTs can be distinguished via the QFI, we map out the excited-state phase diagram by varying the initial CSS. One simple choice is to keep $\rho_m = 0$, $\theta_s = \theta_m = 0$ while varying the value of ρ_0. For such a state the ESQPT lines display a monotonic relation with ρ_0 as $q_c = 2(1 - \rho_0)$ in the positive q region and $q_c = -2\rho_0$ in the negative q region. The preparation of such a CSS can be described by the formula

$$|\zeta\rangle^{\otimes N}_{\text{initial}} = \frac{1}{\sqrt{N!}} (e^{i\frac{\theta}{2}\hat{Q}_{yz}} \hat{a}^\dagger_0 e^{-i\frac{\theta}{2}\hat{Q}_{yz}})^N |\text{vac}\rangle, \tag{4}$$

with $\cos\theta = \sqrt{\rho_0}$ and $\sin\theta = \sqrt{1 - \rho_0}$. In experiments, Eq. (4) corresponds to a process in which one could first prepare the atoms in the $m = 0$ hyperfine state and then apply a combination of magnetic field ramps and resonant radio-frequency (rf) pulses [72] to implement polar-state rotation using the quadrupole operator $\hat{Q}_{yz}$. Using the value of F_Q in the long-time limit at $ct = 10^3$, the excited-state phase diagram is mapped out in the q-ρ_0 plane, as shown in Fig. 2(c). The vertical axis of ρ_0 is reversed in the right half ($q > 0$) with respect to the left half ($q < 0$) in order to make a comparison with the phase diagram in Fig. 1(a). The jump discontinuities signaling the ESQPTs (green dashed lines) can be well captured. One can also notice that the QFI in the vicinity of $|q| = 2c$ is typically much smaller than that around $q = 0$, which can be traced to the properties of variance $\Delta\rho_0$ calculated in Fig. 1(a).

As for the DPT in ground states, the QFI in the long-time limit is calculated with initial P or TF state, respectively, which turns out to display a peak value at $q \simeq \pm c/N$, as shown in Fig. 2(d). These QFI peaks correspond to the QPTs of P $\rightarrow$ S and TF $\rightarrow$ S. For the time-averaged order parameter $\overline{\rho_0(t)}|_{t\rightarrow\infty} \equiv \lim_{T\rightarrow\infty} \frac{1}{T}\int_0^T \rho_0(t)dt = \sum_n |c_n|^2 N_0^n/N$, shown as the dashed lines, they do not display any nonanalyticity for the present small-size mesoscopic quantum system.

IV. PROTOCOL FOR PARAMETER ESTIMATION

Despite that in principle the QFI can be measured via performing many-body quantum state tomography, or measuring the excitation rate of a quantum state upon a periodic drive [73–75], it would be complex to implement for a quantum system of hundreds of atoms [39], and the requirement of real-time measure further prevents the feasibility of direct derivation of the QFI. In the estimation theory, the QFI sets the upper bound on the sensitivity of parameter estimation, i.e., $\Delta q \geqslant 1/\sqrt{F_Q(q,t)}$, which is termed as the quantum Cramér-Rao bound [68]. Thus one can get access to the estimation precision $(\Delta q)^{-2}$ through an observable $\hat{O}$ as

$$(\Delta q)^{-2}_{\hat{O}} = \frac{|\partial_q \langle\hat{O}\rangle|^2}{\Delta^2\hat{O}} \leqslant F_Q, \tag{5}$$
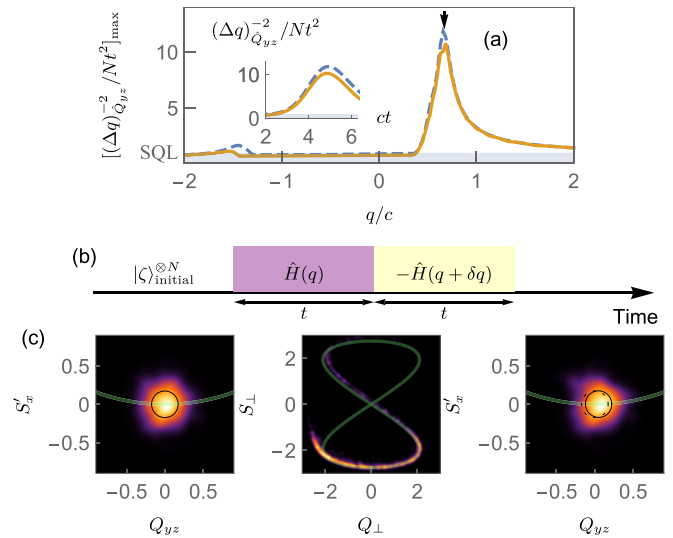

FIG. 3. (a) Maximum of the normalized estimation precision $(\Delta q)^{-2}_{\hat{Q}_{yz}}$ over time as a function of q. The arrow indicates the precision peak around $q \simeq 0.67c$, with the corresponding time evolution shown in the inset. The dashed lines are those for the QFI, which set the upper bound of the precision. (b) Schematic showing the protocol of echo for parameter estimation. (c) Density plot from the truncated Wigner approximation simulation on the inset of (a), where time is chosen to be that the optimal precision is achieved, at $ct \simeq 4.88$. The scale is taken to be 100 atoms and the separatrix is shown in green curve. Left panel: Distribution of the initial CSS on the S'_x-Q_{yz} space with uncertainty ellipse shown in black curve. Middle panel: Distribution on the $S_\perp$-$Q_\perp$ space after the time-forward propagation. Right panel: Distribution at the end of the echo. The uncertainty ellipse (black solid curve) shifts in the Q_{yz} direction as compared with that of the initial state (black dotted curve). All calculations are for $N = 300$.

with $\Delta^2\hat{O} = \langle\hat{O}^2\rangle - \langle\hat{O}\rangle^2$ representing the variance with respect to the initial state $|\psi_0\rangle$. Equation (5) indicates that the value of $(\Delta q)^{-2}_{\hat{O}}$ can approach F_Q with an appropriately chosen observable. SQL corresponds to $(\Delta q)^{-2}_{\text{SQL}} = Nt^2$.

Considering that optimal precision is more likely to be achieved for an observable with small variance, instead of the order parameter $\hat{N}_0$, we propose to use the quadrupole operator $\hat{Q}_{yz}$ as the observable (note that $\hat{Q}_{yz}$ is also found to determine the best precision in a spin-1 condensate interferometry [76]). While $\hat{S}_x$ and $\hat{Q}_{yz}$ construct a pair of observables exhibiting spin-nematic squeezing for an initial P state [77], $\hat{S}'_x = \exp(i\frac{\theta}{2}\hat{Q}_{yz})\hat{S}_x \exp(-i\frac{\theta}{2}\hat{Q}_{yz})$ and $\hat{Q}_{yz}$ are those for the CSS (4) through a unitary transformation [78]. The initial state then constitutes a minimum uncertainty state for $\hat{S}'_x$ and $\hat{Q}_{yz}$, as shown in the left panel of Fig. 3(c). Similar to the definition of the QFI in (2), the precision estimation also invokes an echo process, which is illustrated in Fig. 3(b). We use the truncated Wigner approximation to derive the variation of Q_{yz} after the echo (see Appendix A), from which the maximum values of $(\Delta q)^{-2}_{\hat{Q}_{yz}}$ are found and they synchronize well with the behavior of F_Q, as shown in Fig. 3(a).

In Fig. 3(a) we take the CSS (4) with $\rho_0 = 0.7$ as the initial state. A small deviation between the peaks of $(\Delta q)^{-2}_{\hat{Q}_{yz}}$ and the

mean-field prediction exists, as indicated by the arrow, where the peak locates around $q \simeq 0.67c$ instead of the mean-field critical value of $q_c = 0.6c$, and this can be attributed to the transient and finite-size effects. F_Q can be well approximated by $(\Delta q)_{\hat{Q}_{yz}}^{-2}$, and around the critical q_c the QFI scaling beats the SQL sensitivity $(\Delta q)_{\text{SQL}}^{-2} \sim N$ (see Appendix C for scaling of the QFI). These indicate that a parameter estimation precision beyond SQL can be achieved with the onset of criticality. We have verified that this result remains essentially unchanged when ρ_0 is varied for the initial state, in which the critical points accordingly vary as those have been demonstrated in Fig. 2(c). By varying ρ_0 from 0 to 1, the corresponding q_c varies in the region of $[-2c, 2c]$, with the QFI scaling exponents typically taking a value $\in [1.3, 1.5]$. The precise estimation of the critical q_c can then be extended to a much wider parameter region beyond those at which ground state QPTs take place [61,62].

To understand the physics beneath the enhanced sensing, we explore the echo process during which $(\Delta q)_{\hat{Q}_{yz}}^{-2}$ reaches its peak value [the inset of Fig. 3(a)]. After a time-forward evolution under $\hat{H}(q)$, the atomic state is dispersed along the separatrix, with its majority surpassing the saddle point, as shown in the middle panel of Fig. 3(c). Noticeably, part of the quasiprobability distribution even leaves the separatrix and enters into the P' phase space. This is due to that the motion near the separatrix is apt to phase-space mixing [79]. At the end of the echo after experiencing a time-reversing evolution under $\hat{H}(q + \delta q)$, the state approximately recovers the initial CSS [right panel of Fig. 3(c)], with a small shift in the Q_{yz} component (compare the uncertainty ellipse of initial and final states, marked by dotted and solid lines, respectively). A small perturbation in the control parameter [$\delta q = 10^{-3}c$ in Fig. 3(c)] can give rise to non-negligible variation in the observable, and this is rooted in the sensitive dependence of quantum-state evolution in the deformation of the separatrix, which is well captured through an echo process near the critical points.

V. CONCLUSION

In summary, we have shown the existence of QPTs and ESQPTs in an antiferromagnetic spin-1 condensate and demonstrated their correspondence with DPT, which is characterized using the QFI. We propose that DPT with the condensate initially prepared in a CSS can be used to probe the quantum criticality in excited states, which gives rise to a peak value of the QFI. It can also be used to implement sub-SQL estimation on the effective quadratic Zeeman energy q. It is interesting to note that the ground-state phase transitions from symmetry-broken states to the symmetry-restored spin-singlet state can also be indicated by the DPT. Though we have focused on the system of the spinor condensate, the method of exploring ESQPTs presented here can be applied to a broad class of few-mode quantum systems.

ACKNOWLEDGMENTS

APPENDIX A: NUMERICAL METHODS

The phase diagram presented in Fig. 1 is obtained using the exact diagonalization method. Due to the presence of the SO(2) symmetry in the Hamiltonian [80], the generator $\hat{S}_z$ is conserved; i.e., the magnetization M is a conserved quantity. Then the Hamiltonian matrix $\hat{H}$ written in the $|N_0, M\rangle \equiv |N_1 = \frac{N-N_0+M}{2}, N_0, N_{-1} = \frac{N-N_0-M}{2}\rangle$ basis is block diagonal, for which there are $2N + 1$ blocks with the value of M running from $-N$ to N and each block has a dimension $[\frac{N-M}{2} + 1] \times [\frac{N-M}{2} + 1]$ (here $[\cdot]$ means taking the integer part). Each block matrix is tridiagonal and can be diagonalized separately, and in Fig. 1 a block matrix with $M = 0$ is dealt with.

To simulate the quantum Fisher information presented in Fig. 2 we compute the time-evolved state $|\psi(q, t)\rangle$ with eigenstate expansion. The initial state of the system is described by a coherent spin state $|\zeta\rangle^{\otimes N}$ with (assuming $\rho_{+1} = \rho_{-1}$)

$$\zeta = \begin{pmatrix} \zeta_{+1} \\ \zeta_0 \\ \zeta_{-1} \end{pmatrix} = \begin{pmatrix} \sqrt{\frac{1-\rho_0}{2}} e^{i\phi_{+1}} \\ \sqrt{\rho_0} e^{i\phi_0} \\ \sqrt{\frac{1-\rho_0}{2}} e^{i\phi_{-1}} \end{pmatrix}, \tag{A1}$$

where equal population in the spin-± 1 sublevels is assumed. $|\zeta\rangle^{\otimes N}$ can be written in the Fock basis as

$$|\zeta\rangle^{\otimes N} = \frac{1}{\sqrt{N!}} (\zeta_{+1} \hat{a}_{+1}^\dagger + \zeta_0 \hat{a}_0^\dagger + \zeta_{-1} \hat{a}_{-1}^\dagger)^N |0\rangle, \tag{A2}$$

which can be expanded in the Fock basis $|N_0, M\rangle$ as $|\zeta\rangle^{\otimes N} = \sum_{N_0, M} f(N_0, M) |N_0, M\rangle$ with the coefficient

$$f(N_0, M) = \sqrt{\frac{N!}{N_1! N_0! N_{-1}!}} \left(\sqrt{\frac{1-\rho_0}{2}} \right)^{N-N_0} (\sqrt{\rho_0})^{N_0}$$
$$\times \exp\left[i(N_1 \phi_{+1} + N_0 \phi_0 + N_{-1} \phi_{-1}) \right]. \tag{A3}$$

Some spin operators such as $\hat{Q}_{yz}$ couple blocks of different M, which makes the matrix size very large and it is inconvenient to perform simulation. We adopt truncated the Wigner approximation to study the dynamics [81–84] and obtain the results presented in Fig. 3. The truncated Wigner approximation states that the Wigner function W for a quantum state approximately follows the equation

$$i\hbar \frac{\partial W}{\partial t} \simeq \{H_W, W\}_C, \tag{A4}$$

where H_W is the Wigner-Weyl transform of the Hamiltonian, and $\{\cdots\}_C$ is the coherent-state Poisson bracket. Similarly in the coherent-state picture we treat the operators $\hat{a}_j$ ($\hat{a}_j^\dagger$) as complex c-numbers α_j (α_j^*), and making Wigner-Weyl transform to the Heisenberg equations we have

$$i\hbar \frac{\partial \alpha_j}{\partial t} \simeq \{\alpha_j, H_W\}_C = \frac{\partial H_W}{\partial \alpha_j^*}. \qquad (A5)$$

The truncated Wigner approximation then invokes first sampling the Wigner distribution W with many sets of $\{\alpha_j, \alpha_j^*\}$, and then for each set we solve the equation of motion (A5). Any observable of interest is obtained from the ensemble average. To sample $|\zeta\rangle^{\otimes N}$, we first sample the polar state $\frac{1}{\sqrt{N!}}\hat{a}_0^{\dagger N}|\text{vac}\rangle$ with

$$\begin{pmatrix} \alpha_1 \\ \alpha_0 \\ \alpha_{-1} \end{pmatrix} = \begin{pmatrix} (a+ib)/2 \\ (e+f\eta)e^{i2\pi\xi} \\ (c+id)/2 \end{pmatrix}, \qquad (A6)$$

where a, b, c, d, η are independent random numbers drawn from a Gaussian distribution with zero mean and unit variance, while ξ is a random number drawn from uniform distribution in [0, 1], and [85]

$$e = \frac{1}{2}\sqrt{2N+1+2\sqrt{N^2+N}}, \ f = \frac{1}{4e}. \qquad (A7)$$

Unitary transformation to the coherent spin state is equivalent to performing the rotation

$$\begin{pmatrix} \frac{\cos\theta+1}{2} & \frac{\sin\theta}{\sqrt{2}} & \frac{\cos\theta-1}{2} \\ -\frac{\sin\theta}{\sqrt{2}} & \cos\theta & -\frac{\sin\theta}{\sqrt{2}} \\ \frac{\cos\theta-1}{2} & \frac{\sin\theta}{\sqrt{2}} & \frac{\cos\theta+1}{2} \end{pmatrix} \begin{pmatrix} \alpha_1 \\ \alpha_0 \\ \alpha_{-1} \end{pmatrix} \qquad (A8)$$

with $\cos\theta = \sqrt{\rho_0}$ and $\sin\theta = \sqrt{1-\rho_0}$.

We sample a system of $N = 300$ with 1000 trajectories. It has been compared with the exact quantum mechanical calculations regarding the expectation values and variances of different spin operators, where good agreements are found. The truncated Wigner approximation is capable of simulating quantum dynamics on a short timescale, which is enough for us to produce Fig. 3 in the main text. However it will deviate significantly from the exact quantum mechanical calculations when the evolution time becomes large, due to the omitted high-order terms.

APPENDIX B: SECULAR APPROXIMATION OF THE QUANTUM FISHER INFORMATION

The quantum Fisher information (QFI) can be written in a tensor form as [86]

$$F_Q(q, t) = 4(\langle\partial_q\psi|\partial_q\psi\rangle - |\langle\psi|\partial_q\psi\rangle|^2), \qquad (B1)$$

where $|\psi\rangle = |\psi(q, t)\rangle = e^{-i\hat{H}t}|\psi_0\rangle$. If $\hat{H} = q\hat{H}_q$, one can immediately realize that $F_Q(q, t) = 4t^2\Delta^2\hat{H}_q$ with the variance $\Delta^2\hat{H}_q = \langle\psi_0|\hat{H}_q^2|\psi_0\rangle - |\langle\psi_0|\hat{H}_q|\psi_0\rangle|^2$. Recognizing

$\hat{H} = \hat{H}_0 + q\hat{H}_q$ and $[\hat{H}_0, \hat{H}_q] \neq 0$, we use the identity [87]

$$\exp(i\hat{H}t)\frac{\partial}{\partial q}\exp(-i\hat{H}t)$$
$$= -i\int_0^t dt' \exp(i\hat{H}t')\frac{\partial\hat{H}}{\partial q}\exp(-i\hat{H}t')$$
$$= -i\hat{\mathcal{H}}_q, \qquad (B2)$$

where $\hat{\mathcal{H}}_q = \int_0^t dt' \exp(i\hat{H}t')\hat{H}_q\exp(-i\hat{H}t')$ and this leads to $F_Q(q, t) = 4\Delta^2\hat{\mathcal{H}}_q$. Usually, it is not easy to work out the explicit form of $\hat{\mathcal{H}}_q$ except that the Hamiltonian belongs to some special classes [60]. Using the expansion $|\psi_0\rangle = \sum_n c_n|\psi_n\rangle$, in which $|\psi_n\rangle$ is the eigenstate of $\hat{H}$ with the corresponding eigenenergy E_n, we can get

$$F_Q(q, t) = 4t^2 \left[\sum_n \left| \sum_m c_m H_q^{nm} \text{sinc}\left(\frac{E_{nm}t}{2}\right)e^{iE_{nm}t/2} \right|^2 \right.$$
$$\left. - \left| \sum_{n,m} c_n^* c_m H_q^{nm} \text{sinc}\left(\frac{E_{nm}t}{2}\right)e^{iE_{nm}t/2} \right|^2 \right], \quad (B3)$$

where $E_{nm} = E_n - E_m$. In the long-time limit, the sinc function gives the value of 1 with $E_{nm} = 0$ and zero otherwise. Using an assumption that only the terms with $E_{nm} = 0$ survive in the $t \to \infty$ limit [64] and considering the fact that the spectrum of $\hat{H}$ is nondegenerate, the QFI (B3) can be approximated by (3).

We found out that the approximation is quantitatively valid in a moderately long time. From the viewpoint of phase-space mixing [79], a distribution in phase space will eventually mix up in the energy region it could reach, which will reduce its distinguishability. The distinguishability of a quantum state with respect to the change of Hamiltonian parameters, as characterized by the QFI, is also expected to become coarse in the long-time run.

APPENDIX C: SCALING OF THE QUANTUM FISHER INFORMATION

As the standard quantum limit (SQL) corresponds to $\Delta q = 1/\sqrt{N}$ while in the Heisenberg limit $\Delta q = 1/N$, it is important to know the scaling of the QFI with system size for understanding whether the dynamical phase transition corresponding to excited-state quantum phase transition can be used to implement criticality-enhanced sensing beyond the SQL. The properties of the initial state and associated phase transitions play a central role in dynamical phase transitions, and thus also affect the QFI scaling. Here we illustrate this with the example studied in the main text; i.e., the system is prepared in an initial coherent spin state with $\{\rho_0 = 0.7, \rho_m = 0, \theta_s = \theta_m = 0\}$. With this initial state, the dynamical phase transitions corresponding to excited-state quantum phase transitions are expected to take place at $q_c = -1.4c$ and $0.6c$ in the $N \to \infty$ limit.

We then study the QFI scaling around these two critical points. The results are demonstrated in Fig. 4(a), in which the maximum QFI (dots linked by solid lines) are numerically derived around critical points of $q_c = -1.4c$ (square)
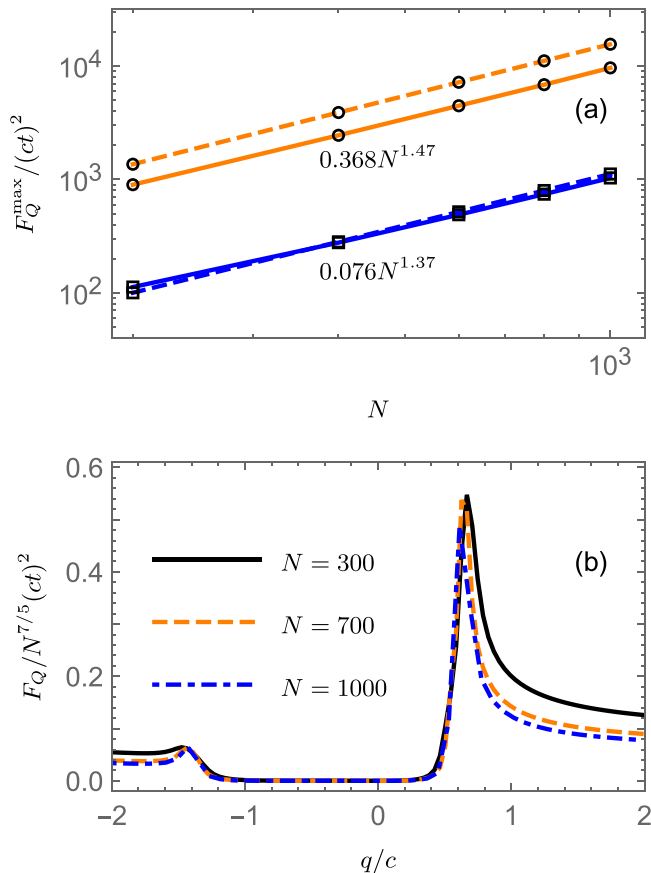
FIG. 4. Scaling of the QFI. (a) F_Q^{max} versus N around $q_c = -1.4c$ (square) and $q_c = 0.6c$ (circle). The numerical and analytical results are represented by those linked by solid and dashed lines, respectively. (b) F_Q scaled by $N^{7/5}$ as a function of q.

and $q_c = 0.6c$ (circle) in the long-time limit ($ct = 1000$). Compared with the long-time analytical results predicted by

(3) (dots linked by dashed lines), we found that the scalings around the negative q_c are almost identical. On the other hand, while the analytical QFI is slightly larger than the numerical results around the positive q_c, their scaling behaviors (slope of the line) coincide. The differences between analytical and numerical results are due to the coarse of quantum-state distinguishability in the long-time run, as discussed at the end of Appendix B.

From data fitting on numerical results we extract the scaling exponent of the QFI, which gives the values of 1.37 and 1.47, respectively, for the dynamical phase transitions on the negative and positive q side. That the scaling exponent is larger than 1 indicates the feasibility of achieving a q-estimation precision beyond SQL as $(\Delta q)^{-2} \sim F_Q > (\Delta q)_{SQL}^{-2}$. In Fig. 4(b) we demonstrate the QFI scaling as a function of q. Noticeably, the peak of the QFI shifts to a value larger than the positive q_c for small system size N; this is due to the finite-size effect which has also been illustrated in Fig. 3.

APPENDIX D: EXPERIMENTAL CONSIDERATION

The echo included first evolves an initial state $|\psi_0\rangle$ forward with $\hat{H}(q)$ and then backward with $\hat{H}(q + \delta q)$. To implement this, one needs to reverse the sign of the Hamiltonian $\hat{H} = \hat{H}_0 + q\hat{H}_q$ such that the system can experience time-reversing evolution. In experiments, the sign of the control parameter q can be varied via microwave dressing [65,66,88]. On the other hand, the sign of $\hat{H}_0$ is determined by the spin-dependent interaction coefficient c, which may be reversed via transferring the atoms from the $F = 1$ hyperfine manifold to that of $F = 2$ [89]. Another promising technique that could be exploited is the photon-mediated spin-exchange interaction, which was experimentally realized recently with the aid of a cavity light field [90–92]. Other methods capable of manipulating spin-dependent collision interactions, such as photoassociation [93], also exist.

[1] S. Sachdev, *Quantum Phase Transitions* (Cambridge University Press, 2000).

[2] P. Cejnar, P. Stránský, M. Macek, and M. Kloc, Excited-state quantum phase transitions, J. Phys. A: Math. Theor. **54**, 133001 (2021).

[3] P. Cejnar, M. Macek, S. Heinze, J. Jolie, and J. Dobeš, Monodromy and excited-state quantum phase transitions in integrable systems: Collective vibrations of nuclei, J. Phys. A: Math. Gen. **39**, L515 (2006).

[4] M. Caprio, P. Cejnar, and F. Iachello, Excited state quantum phase transitions in many-body systems, Ann. Phys. **323**, 1106 (2008).

[5] A. L. Corps and A. Relaño, Constant of Motion Identifying Excited-State Quantum Phases, Phys. Rev. Lett. **127**, 130602 (2021).

[6] H. Lipkin, N. Meshkov, and A. Glick, Validity of many-body approximation methods for a solvable model: (I). Exact solutions and perturbation theory, Nucl. Phys. **62**, 188 (1965).

[7] V. Ulyanov and O. Zaslavskii, New methods in the theory of quantum spin systems, Phys. Rep. **216**, 179 (1992).

[8] M. Heyl, A. Polkovnikov, and S. Kehrein, Dynamical Quantum Phase Transitions in the Transverse-Field Ising Model, Phys. Rev. Lett. **110**, 135704 (2013).

[9] M. Heyl, Scaling and Universality at Dynamical Quantum Phase Transitions, Phys. Rev. Lett. **115**, 140602 (2015).

[10] M. Heyl, Dynamical quantum phase transitions: A brief survey, Europhys. Lett. **125**, 26001 (2019).

[11] S. De Nicola, A. A. Michailidis, and M. Serbyn, Entanglement View of Dynamical Quantum Phase Transitions, Phys. Rev. Lett. **126**, 040602 (2021).

[12] S. Vajna and B. Dóra, Topological classification of dynamical phase transitions, Phys. Rev. B **91**, 155127 (2015).

[13] P. Jurcevic, H. Shen, P. Hauke, C. Maier, T. Brydges, C. Hempel, B. P. Lanyon, M. Heyl, R. Blatt, and C. F. Roos, Direct Observation of Dynamical Quantum Phase Transitions in an Interacting Many-Body System, Phys. Rev. Lett. **119**, 080501 (2017).

[14] K. Yang, L. Zhou, W. Ma, X. Kong, P. Wang, X. Qin, X. Rong, Y. Wang, F. Shi, J. Gong, and J. Du, Floquet dynamical quantum phase transitions, Phys. Rev. B **100**, 085308 (2019).

[15] X.-Y. Guo, C. Yang, Y. Zeng, Y. Peng, H.-K. Li, H. Deng, Y.-R. Jin, S. Chen, D. Zheng, and H. Fan, Observation of a Dynamical Quantum Phase Transition by a Superconducting Qubit Simulation, Phys. Rev. Appl. **11**, 044080 (2019).

[16] J. Lang, B. Frank, and J. C. Halimeh, Dynamical Quantum Phase Transitions: A Geometric Picture, Phys. Rev. Lett. **121**, 130603 (2018).

[17] N. Fläschner, D. Vogel, M. Tarnowski, B. S. Rem, D. S. Lühmann, M. Heyl, J. C. Budich, L. Mathey, K. Sengstock, and C. Weitenberg, Observation of dynamical vortices after quenches in a system with topology, Nat. Phys. **14**, 265 (2018).

[18] J. Zhang, G. Pagano, P. W. Hess, A. Kyprianidis, P. Becker, H. Kaplan, A. V. Gorshkov, Z. X. Gong, and C. Monroe, Observation of a many-body dynamical phase transition with a 53-qubit quantum simulator, Nature (London) **551**, 601 (2017).

[19] J. A. Muniz, D. Barberena, R. J. Lewis-Swan, D. J. Young, J. R. Cline, A. M. Rey, and J. K. Thompson, Exploring dynamical phase transitions with cold atoms in an optical cavity, Nature (London) **580**, 602 (2020).

[20] T.-L. Ho and S. K. Yip, Fragmented and Single Condensate Ground States of Spin-1 Bose Gas, Phys. Rev. Lett. **84**, 4031 (2000).

[21] Y. Kawaguchi and M. Ueda, Spinor Bose-Einstein condensates, Phys. Rep. **520**, 253 (2012).

[22] D. M. Stamper-Kurn and M. Ueda, Spinor Bose gases: Symmetries, magnetism, and quantum dynamics, Rev. Mod. Phys. **85**, 1191 (2013).

[23] L. Sadler, J. Higbie, S. Leslie, M. Vengalattore, and D. Stamper-Kurn, Spontaneous symmetry breaking in a quenched ferromagnetic spinor Bose-Einstein condensate, Nature (London) **443**, 312 (2006).

[24] J. Jiang, L. Zhao, M. Webb, and Y. Liu, Mapping the phase diagram of spinor condensates via adiabatic quantum phase transitions, Phys. Rev. A **90**, 023610 (2014).

[25] H.-X. Yang, T. Tian, Y.-B. Yang, L.-Y. Qiu, H.-Y. Liang, A.-J. Chu, C. B. Dağ, Y. Xu, Y. Liu, and L.-M. Duan, Observation of dynamical quantum phase transitions in a spinor condensate, Phys. Rev. A **100**, 013622 (2019).

[26] E. M. Bookjans, A. Vinit, and C. Raman, Quantum Phase Transition in an Antiferromagnetic Spinor Bose-Einstein Condensate, Phys. Rev. Lett. **107**, 195306 (2011).

[27] L. A. Williamson and P. B. Blakie, Universal Coarsening Dynamics of a Quenched Ferromagnetic Spin-1 Condensate, Phys. Rev. Lett. **116**, 025301 (2016).

[28] M. Uhlmann, R. Schützhold, and U. R. Fischer, Vortex Quantum Creation and Winding Number Scaling in a Quenched Spinor Bose Gas, Phys. Rev. Lett. **99**, 120407 (2007).

[29] B. Damski and W. H. Zurek, Dynamics of a Quantum Phase Transition in a Ferromagnetic Bose-Einstein Condensate, Phys. Rev. Lett. **99**, 130402 (2007).

[30] L.-Y. Qiu, H.-Y. Liang, Y.-B. Yang, H.-X. Yang, T. Tian, Y. Xu, and L.-M. Duan, Observation of generalized Kibble-Zurek mechanism across a first-order quantum phase transition in a spinor condensate, Sci. Adv. **6**, eaba7292 (2020).

[31] X.-Y. Luo, Y.-Q. Zou, L.-N. Wu, Q. Liu, M.-F. Han, M. K. Tey, and L. You, Deterministic entanglement generation from driving through quantum phase transitions, Science **355**, 620 (2017).

[32] Y.-Q. Zou, L.-N. Wu, Q. Liu, X.-Y. Luo, S.-F. Guo, J.-H. Cao, M. K. Tey, and L. You, Beating the classical precision limit

with spin-1 Dicke states of more than 10,000 atoms, Proc. Natl. Acad. Sci. USA **115**, 6381 (2018).

[33] C. B. Dağ, S.-T. Wang, and L.-M. Duan, Classification of quench-dynamical behaviors in spinor condensates, Phys. Rev. A **97**, 023603 (2018).

[34] T. Tian, H.-X. Yang, L.-Y. Qiu, H.-Y. Liang, Y.-B. Yang, Y. Xu, and L.-M. Duan, Observation of Dynamical Quantum Phase Transitions with Correspondence in an Excited State Phase Diagram, Phys. Rev. Lett. **124**, 043001 (2020).

[35] P. Feldmann, C. Klempt, A. Smerzi, L. Santos, and M. Gessner, Interferometric Order Parameter for Excited-State Quantum Phase Transitions in Bose-Einstein Condensates, Phys. Rev. Lett. **126**, 230602 (2021).

[36] J. Cabedo, J. Claramunt, and A. Celi, Dynamical preparation of stripe states in spin-orbit-coupled gases, Phys. Rev. A **104**, L031305 (2021).

[37] J. Cabedo and A. Celi, Excited-state quantum phase transitions in spin-orbit-coupled Bose gases, Phys. Rev. Res. **3**, 043215 (2021).

[38] L. Zhao, J. Jiang, T. Tang, M. Webb, and Y. Liu, Dynamics in spinor condensates tuned by a microwave dressing field, Phys. Rev. A **89**, 023608 (2014).

[39] B. Evrard, A. Qu, J. Dalibard, and F. Gerbier, Observation of fragmentation of a spinor Bose-Einstein condensate, Science **373**, 1340 (2021).

[40] C. K. Law, H. Pu, and N. P. Bigelow, Quantum Spins Mixing in Spinor Bose-Einstein Condensates, Phys. Rev. Lett. **81**, 5257 (1998).

[41] S. Peotta, F. Brange, A. Deger, T. Ojanen, and C. Flindt, Determination of Dynamical Quantum Phase Transitions in Strongly Correlated Many-Body Systems Using Loschmidt Cumulants, Phys. Rev. X **11**, 041018 (2021).

[42] T. Gorin, T. Prosen, T. H. Seligman, and M. Žnidarič, Dynamics of Loschmidt echoes and fidelity decay, Phys. Rep. **435**, 33 (2006).

[43] P. Pérez-Fernández, A. Relaño, J. M. Arias, J. Dukelsky, and J. E. García-Ramos, Decoherence due to an excited-state quantum phase transition in a two-level boson model, Phys. Rev. A **80**, 032111 (2009).

[44] A. Relaño, J. M. Arias, J. Dukelsky, J. E. García-Ramos, and P. Pérez-Fernández, Decoherence as a signature of an excited-state quantum phase transition, Phys. Rev. A **78**, 060102(R) (2008).

[45] T. Macrì, A. Smerzi, and L. Pezzè, Loschmidt echo for quantum metrology, Phys. Rev. A **94**, 010102(R) (2016).

[46] P. Zanardi, M. G. A. Paris, and L. Campos Venuti, Quantum criticality as a resource for quantum estimation, Phys. Rev. A **78**, 042105 (2008).

[47] M. M. Rams, P. Sierant, O. Dutta, P. Horodecki, and J. Zakrzewski, At the Limits of Criticality-Based Quantum Metrology: Apparent Super-Heisenberg Scaling Revisited, Phys. Rev. X **8**, 021022 (2018).

[48] D.-S. Ding, Z.-K. Liu, B.-S. Shi, G.-C. Guo, K. Mølmer, and C. S. Adams, Enhanced metrology at the critical point of a many-body Rydberg atomic system, Nat. Phys. **18**, 1447 (2022).

[49] C. Invernizzi, M. Korbman, L. Campos Venuti, and M. G. A. Paris, Optimal quantum estimation in spin systems at criticality, Phys. Rev. A **78**, 042106 (2008).

[50] P. A. Ivanov and D. Porras, Adiabatic quantum metrology with strongly correlated quantum optical systems, Phys. Rev. A **88**, 023803 (2013).

[51] M. Tsang, Quantum transition-edge detectors, Phys. Rev. A **88**, 021801(R) (2013).

[52] G. Salvatori, A. Mandarino, and M. G. A. Paris, Quantum metrology in Lipkin-Meshkov-Glick critical systems, Phys. Rev. A **90**, 022111 (2014).

[53] K. Macieszczak, M. Gută, I. Lesanovsky, and J. P. Garrahan, Dynamical phase transitions as a resource for quantum enhanced metrology, Phys. Rev. A **93**, 022103 (2016).

[54] T. L. Heugel, M. Biondi, O. Zilberberg, and R. Chitra, Quantum Transducer Using a Parametric Driven-Dissipative Phase Transition, Phys. Rev. Lett. **123**, 173601 (2019).

[55] L. Garbe, M. Bina, A. Keller, M. G. A. Paris, and S. Felicetti, Critical Quantum Metrology with a Finite-Component Quantum Phase Transition, Phys. Rev. Lett. **124**, 120504 (2020).

[56] T. Ilias, D. Yang, S. F. Huelga, and M. B. Plenio, Criticality-enhanced quantum sensing via continuous measurement, PRX Quantum **3**, 010354 (2022).

[57] L. Garbe, O. Abah, S. Felicetti, and R. Puebla, Critical quantum metrology with fully-connected models: From Heisenberg to Kibble-Zurek scaling, Quantum Sci. Technol. **7**, 035010 (2022).

[58] K. Gietka, L. Ruks, and T. Busch, Understanding and improving critical metrology. Quenching superradiant light-matter systems beyond the critical point, Quantum **6**, 700 (2022).

[59] E. Aybar, A. Niezgoda, S. S. Mirkhalaf, M. W. Mitchell, D. B. Orenes, and E. Witkowska, Critical quantum thermometry and its feasibility in spin systems, Quantum **6**, 808 (2022).

[60] Y. Chu, S. Zhang, B. Yu, and J. Cai, Dynamic Framework for Criticality-Enhanced Quantum Sensing, Phys. Rev. Lett. **126**, 010502 (2021).

[61] S. S. Mirkhalaf, E. Witkowska, and L. Lepori, Supersensitive quantum sensor based on criticality in an antiferromagnetic spinor condensate, Phys. Rev. A **101**, 043609 (2020).

[62] S. S. Mirkhalaf, D. Benedicto Orenes, M. W. Mitchell, and E. Witkowska, Criticality-enhanced quantum sensing in ferromagnetic Bose-Einstein condensates: Role of readout measurement and detection noise, Phys. Rev. A **103**, 023317 (2021).

[63] A. Sala, D. L. Núñez, J. Martorell, L. De Sarlo, T. Zibold, F. Gerbier, A. Polls, and B. Juliá-Díaz, Shortcut to adiabaticity in spinor condensates, Phys. Rev. A **94**, 043623 (2016).

[64] Q. Guan and R. J. Lewis-Swan, Identifying and harnessing dynamical phase transitions for quantum-enhanced sensing, Phys. Rev. Res. **3**, 033199 (2021).

[65] F. Gerbier, A. Widera, S. Fölling, O. Mandel, and I. Bloch, Resonant control of spin dynamics in ultracold quantum gases by microwave dressing, Phys. Rev. A **73**, 041602(R) (2006).

[66] S. R. Leslie, J. Guzman, M. Vengalattore, J. D. Sau, M. L. Cohen, and D. M. Stamper-Kurn, Amplification of fluctuations in a spinor Bose-Einstein condensate, Phys. Rev. A **79**, 043631 (2009).

[67] K. Murata, H. Saito, and M. Ueda, Broken-axisymmetry phase of a spin-1 ferromagnetic Bose-Einstein condensate, Phys. Rev. A **75**, 013607 (2007).

[68] S. L. Braunstein and C. M. Caves, Statistical Distance and the Geometry of Quantum States, Phys. Rev. Lett. **72**, 3439 (1994).

[69] S. Pang and T. A. Brun, Quantum metrology for a general Hamiltonian parameter, Phys. Rev. A **90**, 022117 (2014).

[70] T. M. Hoang, C. S. Gerving, B. J. Land, M. Anquez, C. D. Hamley, and M. S. Chapman, Dynamic Stabilization of a Quantum Many-Body Spin System, Phys. Rev. Lett. **111**, 090403 (2013).

[71] W. Zhang, D. L. Zhou, M.-S. Chang, M. S. Chapman, and L. You, Coherent spin mixing dynamics in a spin-1 atomic condensate, Phys. Rev. A **72**, 013602 (2005).

[72] B. Evrard, A. Qu, J. Dalibard, and F. Gerbier, Coherent seeding of the dynamics of a spinor Bose-Einstein condensate: From quantum to classical behavior, Phys. Rev. A **103**, L031302 (2021).

[73] T. Ozawa and N. Goldman, Extracting the quantum metric tensor through periodic driving, Phys. Rev. B **97**, 201117(R) (2018).

[74] T. Ozawa and N. Goldman, Probing localization and quantum geometry by spectroscopy, Phys. Rev. Res. **1**, 032019(R) (2019).

[75] M. Yu, Y. Liu, P. Yang, M. Gong, Q. Cao, S. Zhang, H. Liu, M. Heyl, T. Ozawa, N. Goldman, and J. Cai, Quantum Fisher information measurement and verification of the quantum Cramér-Rao bound in a solid-state qubit, npj Quantum Inf. **8**, 56 (2022).

[76] A. Niezgoda, D. Kajtoch, J. Dziekańska, and E. Witkowska, Optimal quantum interferometry robust to detection noise using spin-1 atomic condensates, New J. Phys. **21**, 093037 (2019).

[77] C. D. Hamley, C. Gerving, T. Hoang, E. Bookjans, and M. S. Chapman, Spin-nematic squeezed vacuum in a quantum gas, Nat. Phys. **8**, 305 (2012).

[78] E. Yukawa, M. Ueda, and K. Nemoto, Classification of spin-nematic squeezing in spin-1 collective atomic systems, Phys. Rev. A **88**, 033629 (2013).

[79] R. Mathew and E. Tiesinga, Phase-space mixing in dynamically unstable, integrable few-mode quantum systems, Phys. Rev. A **96**, 013604 (2017).

[80] Y. Kawaguchi and M. Ueda, Symmetry classification of spinor Bose-Einstein condensates, Phys. Rev. A **84**, 053616 (2011).

[81] P. Blakie, A. Bradley, M. Davis, R. Ballagh, and C. Gardiner, Dynamics and statistical mechanics of ultra-cold Bose gases using c-field techniques, Adv. Phys. **57**, 363 (2008).

[82] A. Polkovnikov, Phase space representation of quantum dynamics, Ann. Phys. **325**, 1790 (2010).

[83] J. Schachenmayer, A. Pikovski, and A. M. Rey, Many-Body Quantum Spin Dynamics with Monte Carlo Trajectories on a Discrete Phase Space, Phys. Rev. X **5**, 011022 (2015).

[84] A. Sinatra, C. Lobo, and Y. Castin, The truncated Wigner method for Bose-condensed gases: Limits of validity and applications, J. Phys. B: At. Mol. Opt. Phys. **35**, 3599 (2002).

[85] M. Olsen and A. Bradley, Numerical representation of quantum states in the positive-*P* and Wigner representations, Opt. Commun. **282**, 3924 (2009).

[86] L. Campos Venuti and P. Zanardi, Quantum Critical Scaling of the Geometric Tensors, Phys. Rev. Lett. **99**, 095701 (2007).

[87] R. M. Wilcox, Exponential operators and parameter differentiation in quantum physics, J. Math. Phys. **8**, 962 (1967).

[88] P. Kunkel, M. Prüfer, H. Strobel, D. Linnemann, A. Frölian, T. Gasenzer, M. Gärttner, and M. K. Oberthaler, Spatially distributed multipartite entanglement enables EPR steering of atomic clouds, Science **360**, 413 (2018).

[89] P. Kunkel, M. Prüfer, S. Lannig, R. Rosa-Medina, A. Bonnin, M. Gärttner, H. Strobel, and M. K. Oberthaler, Simultaneous Readout of Noncommuting Collective Spin Observables beyond the Standard Quantum Limit, Phys. Rev. Lett. **123**, 063603 (2019).

[90] E. J. Davis, G. Bentsen, L. Homeier, T. Li, and M. H. Schleier-Smith, Photon-Mediated Spin-Exchange Dynamics of Spin-1 Atoms, Phys. Rev. Lett. **122**, 010405 (2019).

[91] M. A. Norcia, R. J. Lewis-Swan, J. R. K. Cline, B. Zhu, A. M. Rey, and J. K. Thompson, Cavity-mediated collective spin-exchange interactions in a strontium superradiant laser, Science **361**, 259 (2018).

[92] S. J. Masson, M. D. Barrett, and S. Parkins, Cavity QED Engineering of Spin Dynamics and Squeezing in a Spinor Gas, Phys. Rev. Lett. **119**, 213601 (2017).

[93] H. Jing, Y. Jiang, W. Zhang, and P. Meystre, Laser-catalyzed spin-exchange process in a Bose-Einstein condensate, Phys. Rev. A **81**, 031603(R) (2010).